

SUPPLEMENTARY MATERIAL

Article title: Submarine giant pumice: A window into the shallow conduit dynamics of a recent silicic eruption

Authors: *Samuel J. Mitchell¹, Bruce F. Houghton¹, Rebecca J. Carey², Michael Manga³, Kristen E. Fauria⁴, Meghan R. Jones⁴, S. Adam Soule⁴, Chris E. Conway⁵, Zihan Wei⁶, & Thomas Giachetti⁷

Online Resource 1 – *Sample collection and density distributions*

In March-April 2015, an expedition aboard the R/V *Roger Revelle* spent 3 weeks mapping, exploring and sampling the 2012 Havre eruption using the Remotely Operated Vehicle *Jason* and Autonomous Underwater Vehicle *Sentry*. 290 samples were collected using the ROV across the stratigraphic sequences, using the ROV manipulator, push cores, a vacuum pipe and scoops to effectively sample all lava and clastic deposit types. The 29 giant pumice exterior samples were collected using the ROV manipulator by breaking off large fragments from the sides of giant pumice blocks; the full size distribution of the GP unit has not yet been determined. Collected seafloor samples were immediately washed thoroughly and dried at 80°C for over 24 hours.

Giant pumice fragment densities were analyzed following the method of [Houghton and Wilson \(1989\)](#). Fragments 8 – 32 mm in diameter were cleaned again to remove any fine ash from exterior vesicles and then their exteriors finely coated in hydrophobic silicon spray with negligible mass addition. Fragments were numbered in descending size order for every sample, their dry weight measured, and then their submerged wet weight measured relative to a ballast. Analytical uncertainty in density measurements is given by the precision of the mass measurements where ± 2 standard deviations = 30 kg m⁻³. Using Archimedes principle (**Eq. S1**), the density for each clast was acquired.

$$\text{(Eq. S1)} \quad \text{density} = \frac{\text{dry mass}}{\text{dry mass} - \text{wet mass}}$$

For each of 13 samples analyzed, a single fragment was chosen from the modal density bin from each density distribution. Fragments of modal density / vesicularity were then cut, bound with clear epoxy and thin sectioned with a 0.5 μm diamond polish at the Lapidary Facility at UH Mānoa.

Corresponding vesicularities were calculated using a dense rock equivalent (DRE) density of 2380 kg m⁻³ as determined from averaging the bulk density of 28 finely crushed powders acquired through He-pycnometry (one from each giant pumice) (**Figure 2b**). This density value corresponds well with the DRE used in the [Manga et al. \(2018a\)](#) model and previous Kermadec pumice studies: 2400 kg m⁻³ ([Barker et al., 2012](#); [Rotella et al., 2015](#)).

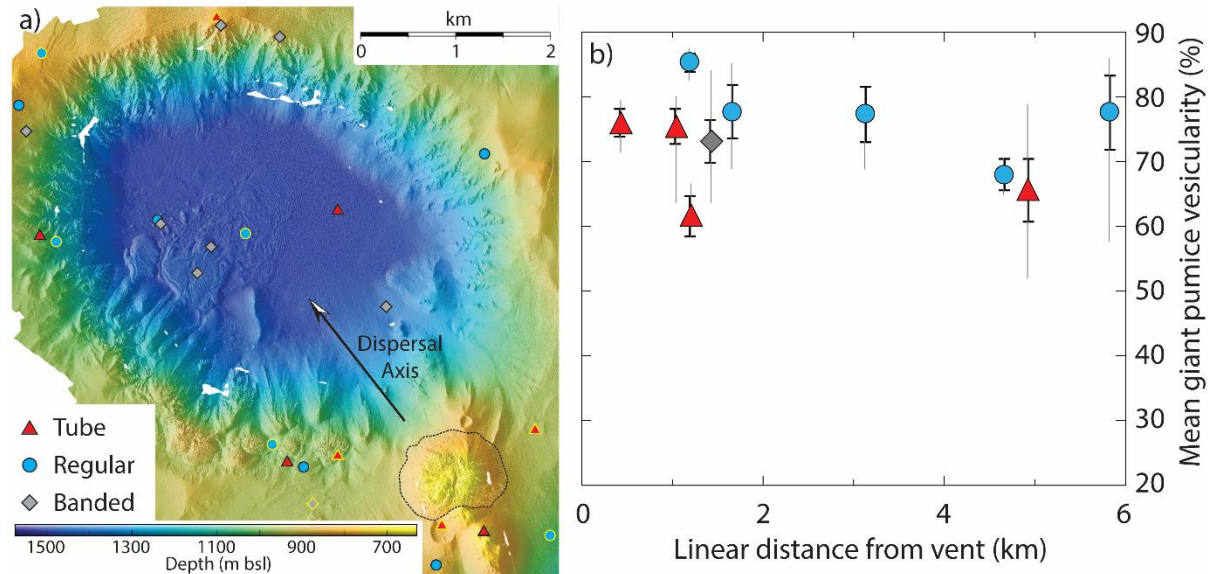


Figure S11: Original location of samples analyzed within this study (a) and the corresponding density distributions of samples studied ‘in-detail’ (b). A textural classification is given for all samples. Samples outlined in yellow (a) correspond to those chosen for more detailed 2D microtextural analysis in (b) and throughout the rest of this study. Giant pumice density distributions of exterior fragments (b) are presented as vesicularity ($DRE = 2380 \text{ kg m}^{-3}$) with clast distance from the vent. The symbol marks the mean, the black error bars represent one standard deviation, and the grey line marks the maximum and minimum vesicularity measured.

(Below) Repository of data and corresponding IGSN numbers for Havre 2012 samples used in this study. Location, unit, macrotextural classification and depth are given for each collected HVR_sample.

IGSN	HVR_sample	Stratigraphic Unit	Classification	In situ depth (m)	Latitude (°)	Longitude (°)
IEHVR0003	003	GP	Tube	944	-31.12352	-179.00642
IEHVR000M	022	“	“	954	-31.12627	-179.02861
IEHVR002V	103	“	“	972	-31.12671	-179.03373
IEHVR0037	115	“	“	844	-31.13238	-179.01682
IEHVR003D	121	“	“	717	-31.13332	-179.01219
IEHVR003P	133	“	“	1513	-31.10265	-179.02862
IEHVR0067	223	“	“	1020	-31.10493	-179.06059
IEHVR007I	270	“	“	801	-31.08457	-179.04110
IEHVR0015	041	“	Regular	1507	-31.10463	-179.03825
IEHVR002O	096	“	“	989	-31.12497	-179.03510
IEHVR002Y	106	“	“	963	-31.12713	-179.03218
IEHVR003H	125	“	“	875	-31.13727	-179.01718
IEHVR004K	164	“	“	1518	-31.09933	-179.04855
IEHVR005C	192	“	“	1012	-31.13414	-179.00538
IEHVR0065	221	“	“	1057	-31.10542	-179.05910
IEHVR006B	227	“	“	852	-31.09300	-179.06230
IEHVR006F	231	“	“	826	-31.08778	-179.06050
IEHVR007T	281	“	“	966	-31.09748	-179.01182
IEHVR0018	044	“	Banded	1482	-31.10747	-179.04341
IEHVR003V	139	“	“	1489	-31.10640	-179.04226
IEHVR004L	165	“	“	1509	-31.10284	-179.04730
IEHVR006A	226	“	“	926	-31.09528	-179.06230
IEHVR006R	243	“	“	1437	-31.11175	-179.02250
IEHVR007F	267	“	“	803	-31.08515	-179.04076
IEHVR007Q	278	“	“	895	-31.08622	-179.03485
IEHVR0082	290 (GP290)	“	“	950	-31.12975	-179.03108

Density distributions from GP samples:

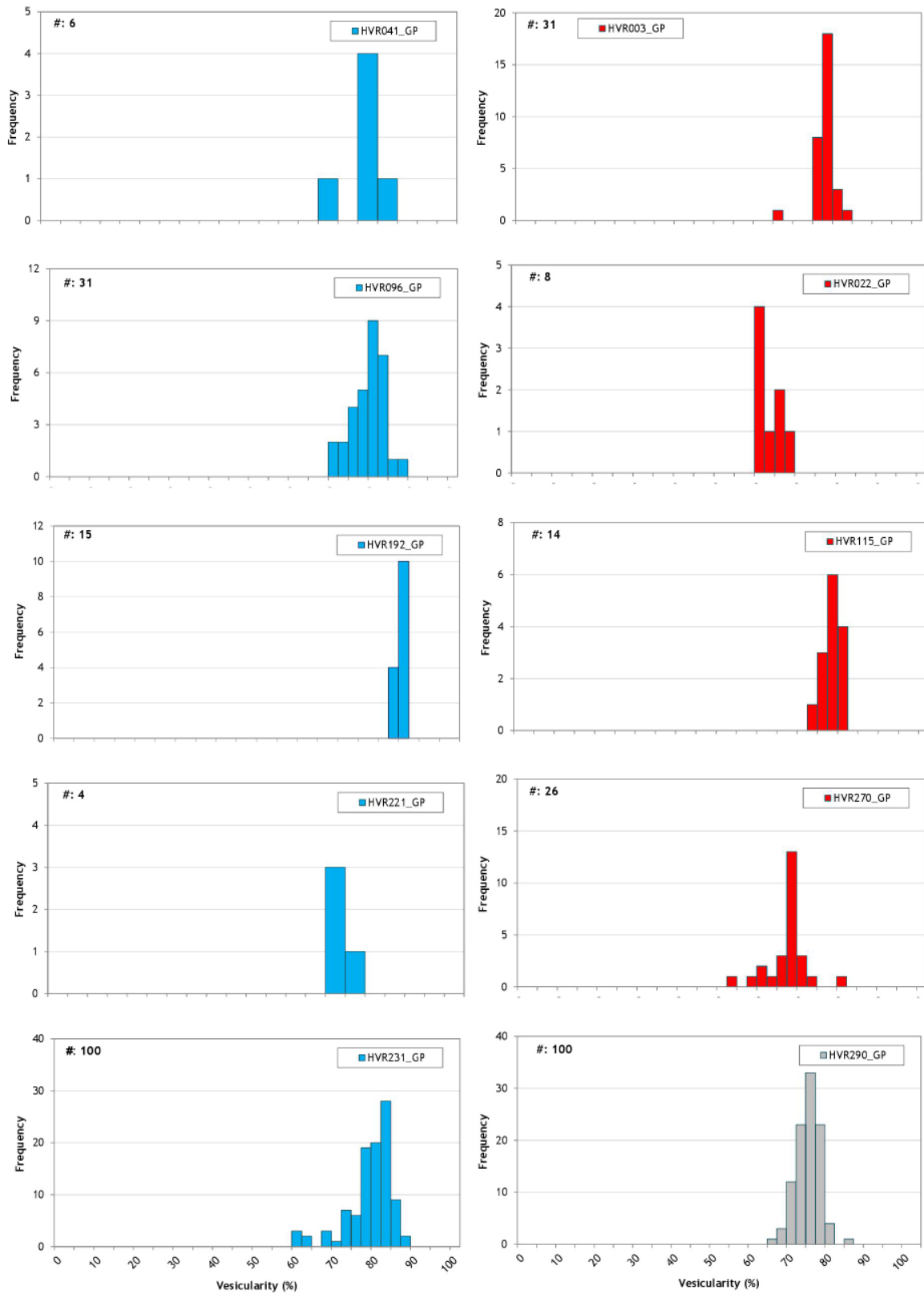
Breakdown of density data from each GP block exterior sampled by *Jason*. *denotes samples with much larger fragments. Sample analysis was limited by the volume of material recovered during sample collection from the seafloor. $\sigma = 1$ standard deviation of error from the mean of the distribution

Sample (HVR_)	Distance from vent (km) (± 0.05)	Density ($\times 10^3 \text{ kg m}^{-3}$)				# fragments analysed
		Mean	1σ	Maximum	Minimum	
3	1.03	0.57	0.06	0.85	0.47	31
22	1.20	0.90	0.07	0.98	0.79	8*
41	3.12	0.53	0.10	0.73	0.43	6*
96	1.65	0.52	0.10	0.73	0.35	31
115	0.42	0.56	0.05	0.67	0.48	14
192	1.19	0.34	0.03	0.41	0.30	15
221	4.65	0.75	0.06	0.82	0.69	4*
231	5.81	0.52	0.13	0.99	0.32	100
270	4.92	0.80	0.11	1.13	0.49	26
290	1.43	0.63	0.08	0.85	0.37	100

References:

- Barker, S. J., Rotella, M. D., Wilson, C. J., Wright, I. C., and Wysoczanski, R. J., 2012, Contrasting pyroclast density spectra from subaerial and submarine silicic eruptions in the Kermadec arc: implications for eruption processes and dredge sampling: *Bulletin of volcanology*, v. 74, no. 6, p. 1425-1443., doi: 10.1007/s00445-012-0604-2
- Houghton, B. F., and Wilson, C., 1989, A vesicularity index for pyroclastic deposits: *Bulletin of volcanology*, v. 51, no. 6, p. 451-462.
- Manga, M., Fauria, K. E., Lin, C., Mitchell, S. J., Jones, M., Conway, C., Degruyter, W., Hosseini, B., Carey, R. J., Cahalan., Houghton, B. F., White, J. D. L., Jutzeler, M., Soule, S. A., and Tani, K., 2018, The pumice raft-forming 2012 Havre submarine eruption was effusive: *Earth and Planetary Science Letters*, 2018.
- Rotella, M. D., Wilson, C. J., Barker, S. J., Schipper, C. I., Wright, I. C., and Wysoczanski, R. J., 2015, Dynamics of deep submarine silicic explosive eruptions in the Kermadec arc, as reflected in pumice vesicularity textures: *Journal of Volcanology and Geothermal Research*, v. 301, p. 314-332., doi: 10.1016/j.jvolgeores.2015.05.021

Figure S1ii: Individual vesicularity distributions for each GP block exterior. Blue = regular, red = tube and grey = banded.



Online Resource 2 – XRF analyses and standards

Pumice samples were prepared for whole-rock geochemical analysis by cutting away altered surfaces, and crushing material to obtain fresh ~1x1 cm pieces, which were washed in running hot water (~50°C) for 7–14 days to leach seawater. Once leached, pieces were broken in an iron mortar into 2–5 mm chips that were then washed in an ultrasonic bath using deionised water and acetone. The cleaned chips were dried in an oven at 110°C for >12 hours and then powdered. Before the major element analysis, 0.4 g of powder was weighed on a Metler Toledo dual balance system and ignited at 1025°C for 4 hours in an electric muffle furnace to determine loss-on-ignition (LOI). After the LOI determination, glass beads containing lithium tetraborate flux (10 to 1 dilution of sample) were prepared. The glass beads (and GP samples) were analyzed by X-ray fluorescence analysis (Rigaku RIX1000) at the National Museum of Nature and Science in Tsukuba, Japan for major elements. Values for analytical precision and accuracy (± 2 standard deviations), as estimated from repeated analysis of well-established reference standard JB-1, are provided in the table below:

Element (wt %)	SiO ₂	TiO ₂	Al ₂ O ₃	Fe ₂ O ₃	MnO	MgO	CaO	Na ₂ O	K ₂ O	P ₂ O ₅
JB-1 average	52.7	1.3	14.4	8.9	0.2	7.9	9.3	2.8	1.5	0.3
2 SD	0.05	0.01	0.02	0.01	0.00	0.001	0.01	0.02	0.00	0.00
JB-1 GeoRem	52.4	1.3	14.5	9.0	0.2	7.7	9.3	2.8	1.4	0.3
% offset	0.55	0.53	-0.7	-0.75	-1.96	2.48	0.68	-0.47	1.4	1.96

Concentrations are given as oxide concentration wt. % for all elements except Cl, S and the trace elements.

XRF analysis of all samples

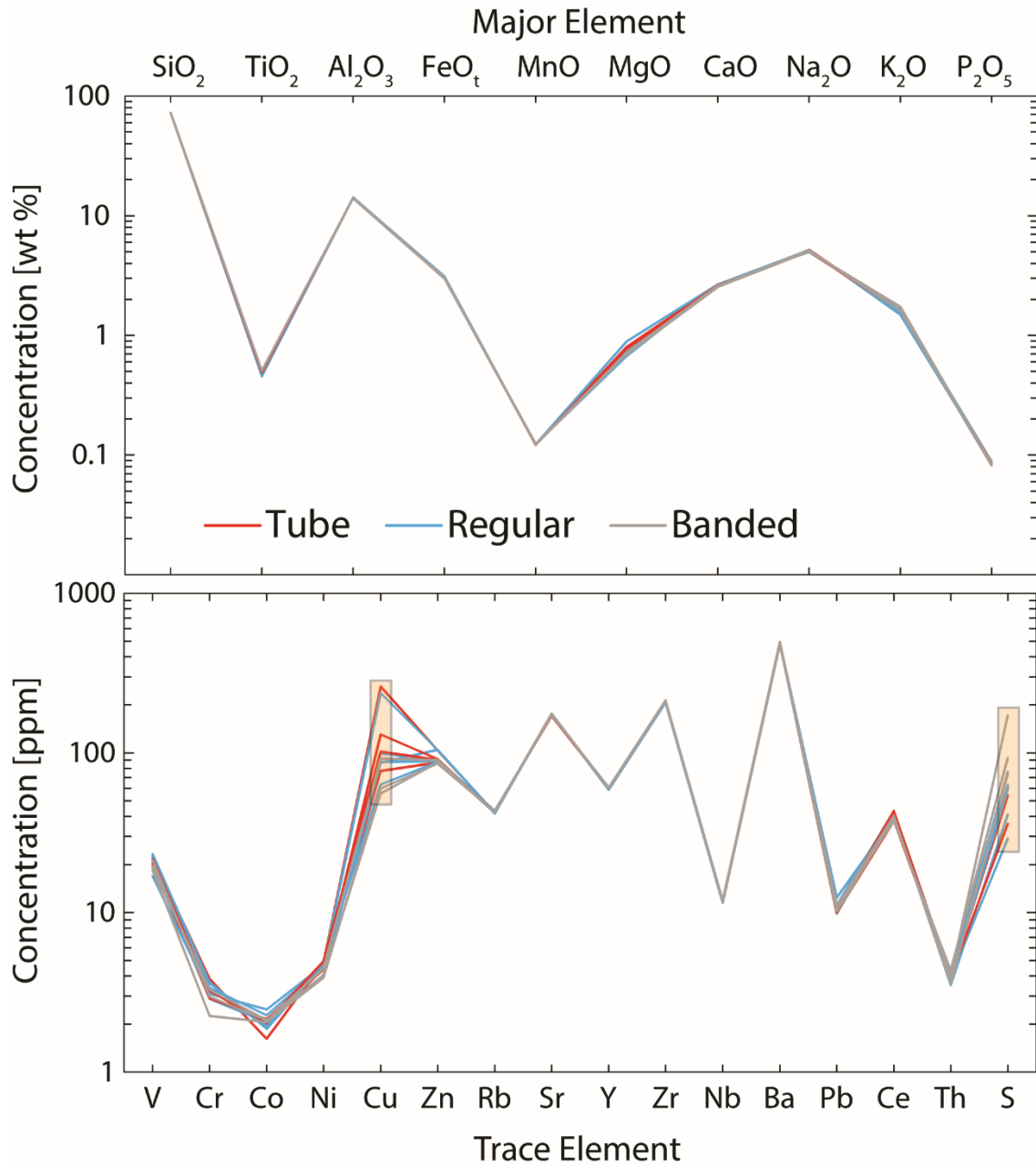


Figure S2i: A compilation of all XRF analyses with major elements normalized to 100 total wt. %. Colored lines correspond to macrotextural classifications. In the trace element plot, orange boxes denote elements with deviation outside of 80% confidence with a 1:1 relationship: Cu and S. S variations are an artifact of low volatilization temperatures during XRF analyses and Cu variations could be the result of hydrothermal alteration on clast exteriors or Cu-rich water diffusing into the glass at higher temperature during rapid rehydration (Mitchell et al., 2018a).

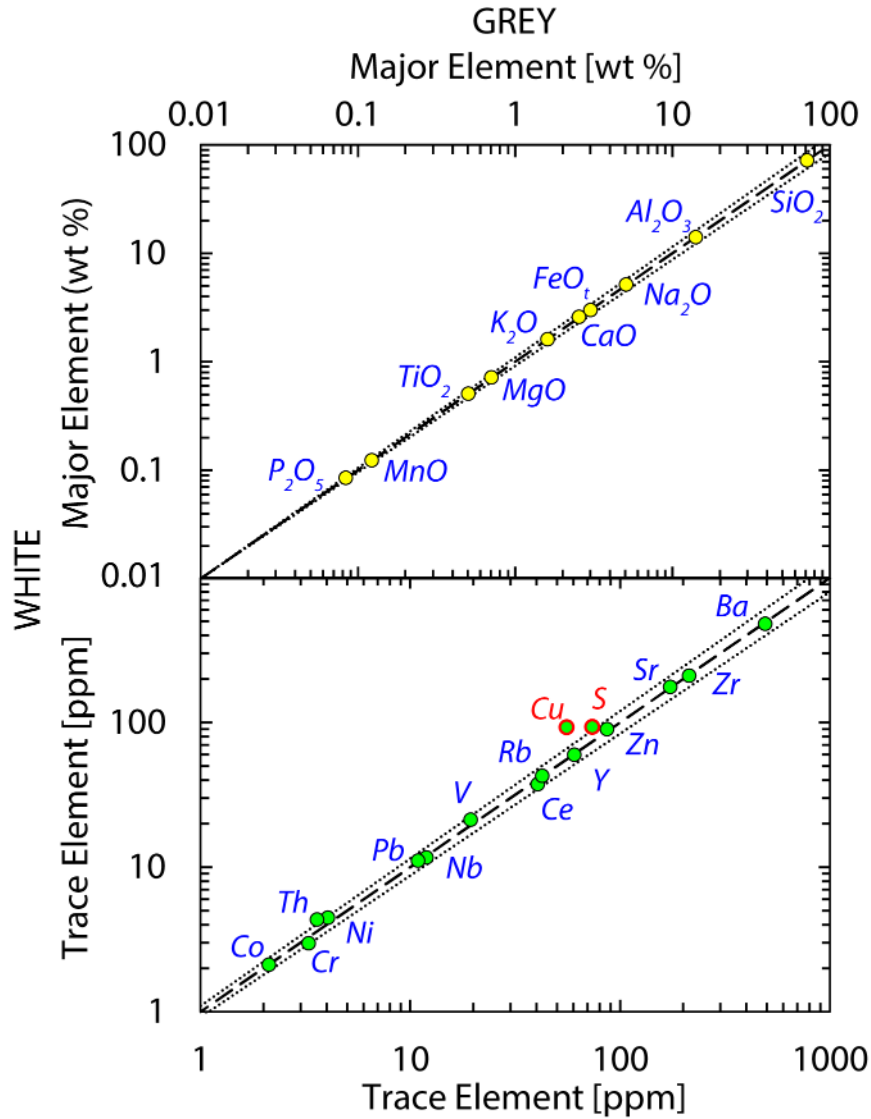


Figure S2ii: A comparison of major, minor and trace element content within adjacent white and grey bands from whole rock XRF analysis of GP290. The dashed line gives a 1:1 relationship with an 80% confidence interval bounded by the dotted lines. Cu and S lie outside of this confidence (highlighted in red).

Trace Element Geochemistry

Raw XRF whole rock minor and trace element geochemistry GP samples. Samples are defined by their HVR_ sample number and macrotextural classification. Iron is corrected to FeO_t from Fe₂O₃. All concentration values are given in ppm.

Group	Regular					Tube				Banded		
HVR_	041	096	192	221	231	003	022	115	270	290	290_Grey	290_White
V	22.46	19.89	23.29	16.95	19.06	22.25	19.57	20.58	21.68	18.51	19.44	19.44
Cr	3.61	2.87	3.66	3.09	3.39	3.86	3.29	2.90	3.23	2.25	3.28	3.28
Co	1.93	2.06	1.87	2.47	2.27	1.62	1.96	2.15	2.04	2.06	2.12	2.12
Ni	4.79	4.06	4.77	4.68	4.65	4.89	4.45	4.41	4.96	3.92	4.05	4.05
Cu	63.53	86.67	236.25	87.85	99.20	260.28	77.18	130.69	101.97	59.85	55.8	55.8
Zn	87.64	104.46	104.78	88.74	90.80	103.74	87.13	91.61	90.41	85.68	86.65	86.65
Rb	42.17	42.21	41.74	42.96	43.37	42.15	43.10	42.73	42.61	42.75	42.72	42.72
Sr	175.72	176.31	174.58	172.93	172.52	174.27	170.50	173.53	174.04	174.93	173.74	173.74
Y	59.38	59.1	58.76	59.96	60.13	59.42	59.96	59.65	59.90	59.94	60.61	60.61
Zr	209.29	206.95	206.72	212.99	213.53	207.85	211.88	210.61	211.94	211.99	213.84	213.84
Nb	11.66	11.62	11.52	11.75	11.82	11.61	11.79	11.68	11.74	11.74	11.94	11.94
Ba	484.89	485.27	479.35	489.45	491.20	485.61	494.03	488.18	483.47	486.29	491.66	491.66
Pb	9.85	12.37	10.96	11.14	10.25	10.08	10.02	9.98	10.40	10.19	10.92	10.92
Ce	40.44	39.44	41.56	43.22	40.61	43.02	37.50	40.73	43.27	38.23	40.46	40.46
Th	3.51	3.91	3.79	4.05	3.85	3.83	3.94	3.95	3.98	3.98	3.59	3.59

Online Resource 3 – EPMA count times

EMPA was accomplished using a JEOL JXA-8500F microprobe analyser with a field-emission electron gun at the University of Hawai’i at Mānoa. Measurements were acquired using 15keV accelerating voltage with a 10 nA beam current and a spot size of 10 µm. Being a highly mobile element, Na was measured prior to other elements assigned to the same spectrometer.

(Below) Count times (seconds) for each element on and off the identified peak to determine background and subsequent true intensity of $k\alpha$ peak in WDS wavescans. These count times were the same for both standard calibration and samples.

Element	Si	Ti	Al	Fe	Mn	Mg	Ca	Na	K	P	Cl	S
On peak time	35	35	65	30	30	65	60	35	30	35	30	30
Off peak high	17.5	17.5	32.5	15	15	32.5	30	17.5	15	17.5	15	15
Off peak low	17.5	17.5	32.5	15	15	32.5	30	17.5	15	17.5	15	15

Online Resource 4 – BSE images processing, nesting and 3D vesicle stereo-conversion

Binary Image Processing

Backscattered electron (BSE) images were acquired using an electron microprobe and processed using the imaging software FijiApp (containing ImageJ). Whole-fragment scans were acquired at 46.5 pixel/mm resolution. All raw BSE images were processed into black and white binary images using Adobe Photoshop where black was vesicles, and white was melt and crystals. For large crystals and phenocrysts, crystals were separated out as grey. Images were “repaired” by: fixing broken thin bubble walls, removing vesicle pits (the very bottom of a vesicle intersection not conducive to any particular vesicle size), filling in vesicles with broken material inside, and strengthening very thin bubble walls to a 3 pixel width (individual objects in FijiApp can only be differentiated with a 3 pixel difference between them). All vesicles were then “decoalesced”, where coalesced vesicles with clear bubble throats were manually separated with three pixels of melt. Extreme levels of bubble coalescence could not be identified if bubble throats were not visible. However, based on a lack of evidence for vesicle collapse and/or relaxation, we suggest that most bubble coalescence is identifiable from the BSE images. Each stage of processing was done within a different layer in Photoshop to track changes and to remove layers if need be e.g. to assess real, un-strengthened bubble wall thicknesses.

In ImageJ, each image was first converted to an 8-bit binary, decoalesced image and then smoothed to remove any one pixel binary impurities. Any incomplete vesicles at the image edge were placed within a “mask” and removed from the binary image to produce an accurate vesicularity area and to remove incomplete vesicles from vesicle size distribution (VSDs). Complete vesicles touching the walls were included within images. Within each image at each magnification, ImageJ measured image area without the mask, image vesicularity, number of vesicles inside the mask, the % fraction of phenocrysts, and the size and shape of all vesicles in each image.

The image nests were the same for all analyses (**Figure S4i**): one full thin section scan at 5× magnification, eight 50× images stitched into two large 50x area, eight 250× images and then, if needed, four 500× images. The diagram below shows the nesting structure with an example of a giant pumice fragment nest where, in each image, the masks have been removed. Only the vesicles analyzed are displayed:

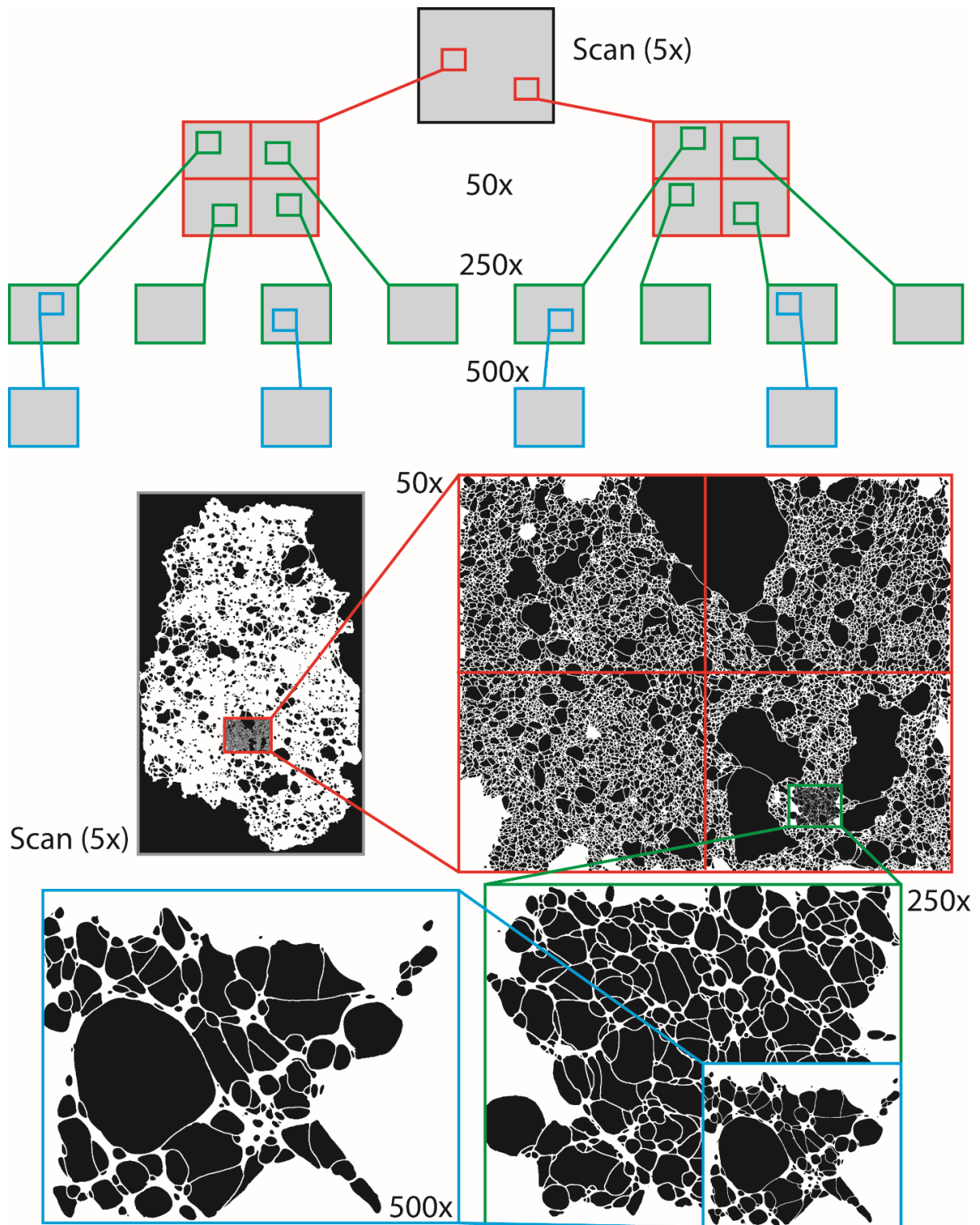


Figure S4i

The 500× images were rarely of additional value to the nest as most vesicles could be accurately analyzed up to 250× i.e. a lack of an extremely microvesicular population. Our cut off for accurate vesicle width was 10 pixels (Shea et al., 2010). Using this image nest structure, we were able to analyze vesicles with equant diameters from 2.4 μm up to 3.78 mm; rarely were thin sections used where vesicles > 4 mm in diameter would skew the analysis. For each

vesicle, the area (A) was converted to an equivalent best-fit ellipse where the circular-equivalent diameter: $EqD = \sqrt{4/\pi A}$. All vesicle sizes within the size distribution are reported as EqD for the later spherical stereo-conversion calculations. VSDs were binned using a $\times 10^{0.1}$ bin factor. This produced 32 geometrically-equivalent bins within the 2.4 μm to 3.78 mm size range. Magnification cutoffs were chosen based on overlaps of VSDs from each magnification where the higher magnification required at least 20 vesicles per total area for one set of magnifications. Using ImageJ, we were able to produce VSDs for each thin section over 32 size bins where vesicle number densities were given as N_A (number vesicles of a given size range for a total magnification area).

2D to 3D bubble stereo-conversion

VSDs and N_A values were then used to determine VVDs and N_V values using a 2D to 3D stereo-conversion assuming a spherical vesicle geometry based on the EqD obtained (Sahagian and Proussevitch, 1998). Each geometric bin of vesicle sizes (N_A value) was converted into an N_V value for the same bin size. Sahagian and Proussevitch (1998) determined the intersection probabilities (P) for spheres of 12 classes with a $10^{0.1}$ geometric bin factor using 10^6 Monte Carlo simulations of planes of variable angles intersecting spheres of various sizes. P values were then converted into conversion coefficients (α) for ease of incorporating P into N_V calculations where j denotes the chosen class number and i denotes the number of classes analyzed:

$$\alpha_i = \frac{1}{P_1} \left(\alpha_1 P_i - \sum_{j=1}^{i-2} \alpha_{j+1} P_{i-j} \right)$$

For the spherical assumption, a logarithmic extrapolation was applied to classes 5 to 12 to extrapolate α values for 32 classes. The extrapolation fit of classes 5 to 12 had $R^2 = 0.9999$ whereas using all 12 classes gave $R^2 = 0.9966$; a small variation but critical when assessing α values over 10 orders of magnitude. Each bin size limit was converted into a volume and then an average to determine a projected mean vesicle height (H)

With H , N_A and α values determined for each of the 32 classes, the 3D stereo-conversion could be applied to obtain vesicle number densities per volume for each geometric bin (N_{Vi}). This calculation is applied to every bin size:

$$N_{Vi} = \frac{1}{H_i} \left(\alpha_1 N_{Ai} - \sum_{j=1}^{i-1} \alpha_{j+1} A_{A(i-j)} \right)$$

The sum of N_{Vi} across all 32 bins gives the total vesicle number density for the entire thin section for vesicle equant diameters of 2.4 μm to 3.78 mm (N_V). All N_V values quoted within this paper are in units of cm^{-3} . N_V values are also corrected for bulk clast vesicularity (ϕ) where:

$$N_{Vm} = \frac{100N_V}{100 - \phi}$$

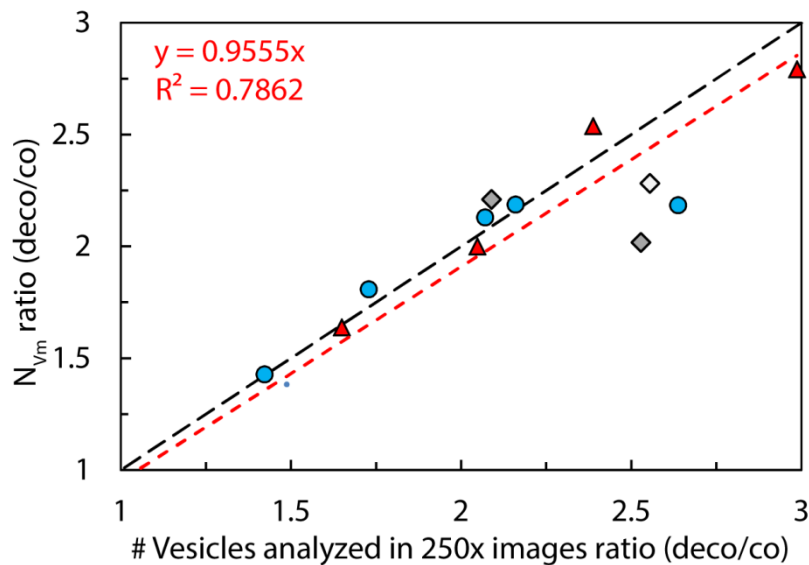
Vesicle volume distributions (VVDs) were determined after the stereo-conversion. Each H value was converted into a volume of the EqD sphere (V_H). The absolute volume fraction of each class (V_i) was simply calculated as $V_i = V_{Hi}N_{Vi}$. These were adjusted by a factor of $\sum V_i$ and subsequently converted into cumulative % volume fraction.

For tube pumices with extremely elongate vesicles, we used previously determined P and α values from [Sahagian and Proussevitch \(1998\)](#) for pre-defined vesicle geometries. The details of this non-spherical stereo-conversion are given within Appendix A.

Bubble decoalescence

To test the subjectivity of manual bubble decoalescence and the effects on resulting vesicle number density values, we determined total N_{Vm} values using both fully decoalesced and coalesced vesicle 250 \times mag. images where the masks and areas analyzed are kept the same. We only used the 250 \times images for this test, as the 5 \times and 50 \times images contribute a negligible addition to N_{Vm} values.

Figure S4ii: For each sample analyzed, we compare to ratio of N_{Vm} after decoalescence to N_{Vm} before decoalescence i.e. coalesced, to the ratio of number of decoalesced vesicles analyzed in all eight 250x images per samples to the number of coalesced vesicles prior to decoalescence:



We observe a strong relationship between the two ratios where it can be seen that decoalescence allows decoalesced N_{Vm} value to remain consistent with the change in number of vesicles. The ratio of coalesced to decoalesced bubbles scales linearly with calculated changes in N_{Vm} and manual decoalescence never more than three-fold.

Vesicle shape analysis

Coalesced vesicles were manually decoalesced across all magnifications for accurate representation of the area, perimeter and shape parameters of individual vesicles during subsequent size and shape analysis. We assess the 2D cross sections of vesicles in BSE images using four main shape parameters commonly used in ash morphology analysis ([Liu et al.](#),

2015): circularity, roundness, regularity and solidity. A is the vesicle area, P is the vesicle perimeter, a is the primary (major) axis of the best-fit ellipse, D_f is Feret's diameter – the longest distance between any two points on the vesicle edge, and A_C is the convex area of the vesicle (Schindelin et al., 2012).

$$\text{Circularity} = \frac{4\pi A}{P^2} \quad (\text{Eq. 2})$$

$$\text{Roundness} = \frac{4A}{\pi a^2} \quad (\text{Eq. 3})$$

$$\text{Regularity} = \frac{a}{D_f} \quad (\text{Eq. 4})$$

$$\text{Solidity} = \frac{A}{A_C} \quad (\text{Eq. 5})$$

For vesicles over $19 \mu\text{m}$ in diameter, we assess the four shape parameters for vesicles in all $250\times$ BSE images; smaller vesicle sizes are too pixelated.

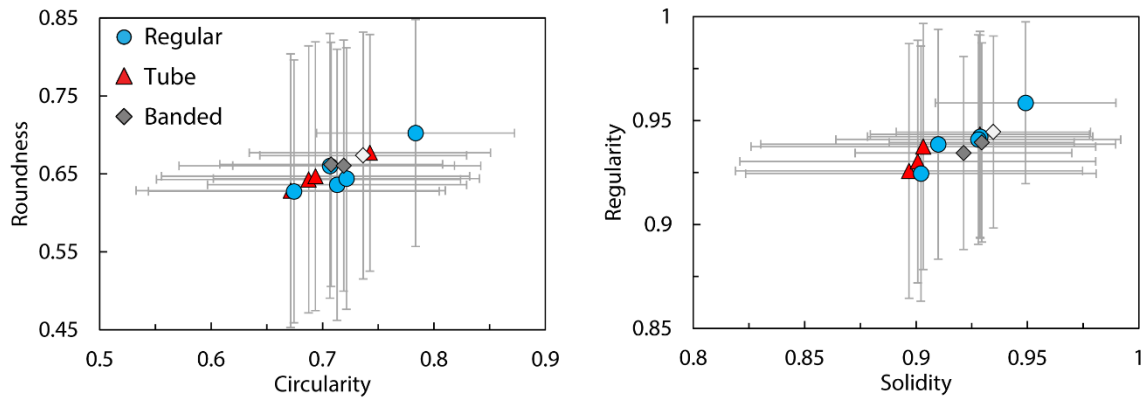
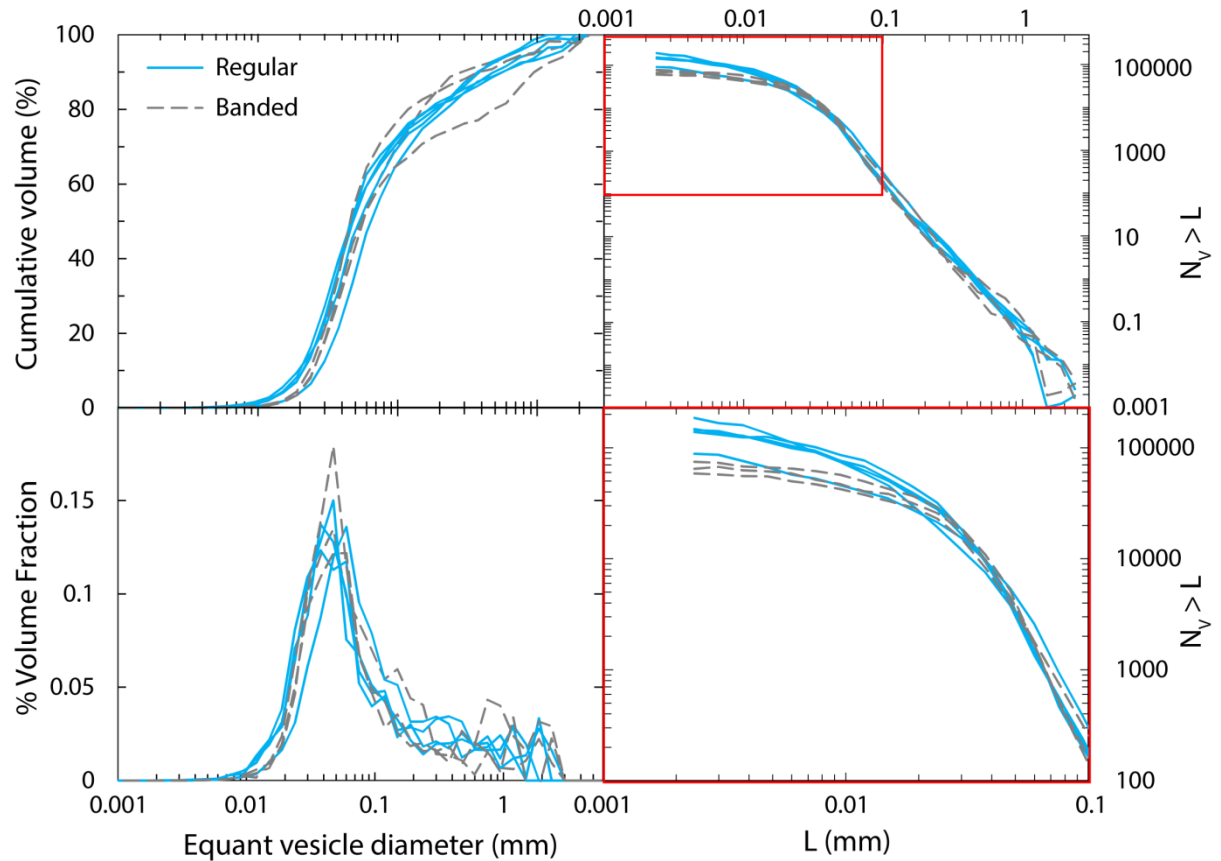


Figure S4iii: Vesicle shape analysis for all vesicles >50 pixels ($19 \mu\text{m}$) in diameter from all $250\times$ magnification images. Four shape factors are compared to display the most significant difference between macrotextural groups: solidity, regularity, roundness and circularity (formula in text). Error bars given are ± 1 standard deviation.

There is no clear distinction between giant pumice macrotextural groups, although one regular giant pumice stands out with very equant and circular vesicles (HVR_221). HVR_221 has notably lower vesicularity likely to be affected by decoalescence and so vesicle shapes remain very circular. Discounting the tube vesicles, a decrease in circularity and regularity may reflect a maturation of bubble textures to the beginning of permeable pathway collapse. We do note that a 2D cross section results in some vesicles not sectioned directly through their diameter and that 3D vesicle orientation will affect the shape results of sheared vesicles (Sahagian and Proussevitch, 1998). We also note that in highly vesicular samples with significant bubble coalescence, manual decoalescence will not preserve original vesicle shape. For this reason, we do not over-interpret the difference between regular, tube and banded giant pumice samples.

Continued N_V and VVD analysis

Figure S4iv: Distribution of volume fraction and number density across vesicles size from 2.4 μm to 3.78 mm for all textural classifications except for tube pumices (as in Figure 8). Cumulative and %-adjusted volume fraction distributions are given in the top plots. The density number of vesicles (N_V) greater than the mid value of each size bin (L) is given in bottom-left with the highest $N_V > L$ values expanded in bottom-right to display the major differences in N_V of vesicles $< 100 \mu\text{m}$ between classifications.



All giant pumice samples have consistent $N_V > L$ trends from $\sim 40 - 500 \mu\text{m}$ where deviations arise as vesicle numbers become very small at large diameters ($> 1 \text{ mm}$). The apparent higher N_{V_m} in regular pumices than banded pumices come from contribution of vesicles $< 20 \mu\text{m}$ except for HVR_192 (the highest vesicularity GP sample) where $N_V > L$ are similar to banded pumices. These differences in small vesicle number densities could allude to differing decompression rates in the shallow conduit between regular and banded pumices.

References:

- Liu, E.J., Cashman, K.V. and Rust, A.C., 2015. Optimising shape analysis to quantify volcanic ash morphology. *GeoResJ*, 8, pp.14-30.
- Sahagian, D. L. and Proussevitch, A. A., 1998. 3D particle size distributions from 2D observations: stereology for natural applications. *Journal of Volcanology and Geothermal Research*, 84(3-4), pp.173-196.
- Schindelin, J., Arganda-Carreras, I., Frise, E., Kaynig, V., Longair, M., Pietzsch, T., Preibisch, S., Rueden, C., Saalfeld, S., Schmid, B. and Tinevez, J. Y., 2012. Fiji: an open-source platform for biological-image analysis. *Nature methods*, 9(7), p.676.
- Shea, T., Houghton, B.F., Gurioli, L., Cashman, K. V., Hammer, J.E., and Hobden, B.J., 2010, Textural studies

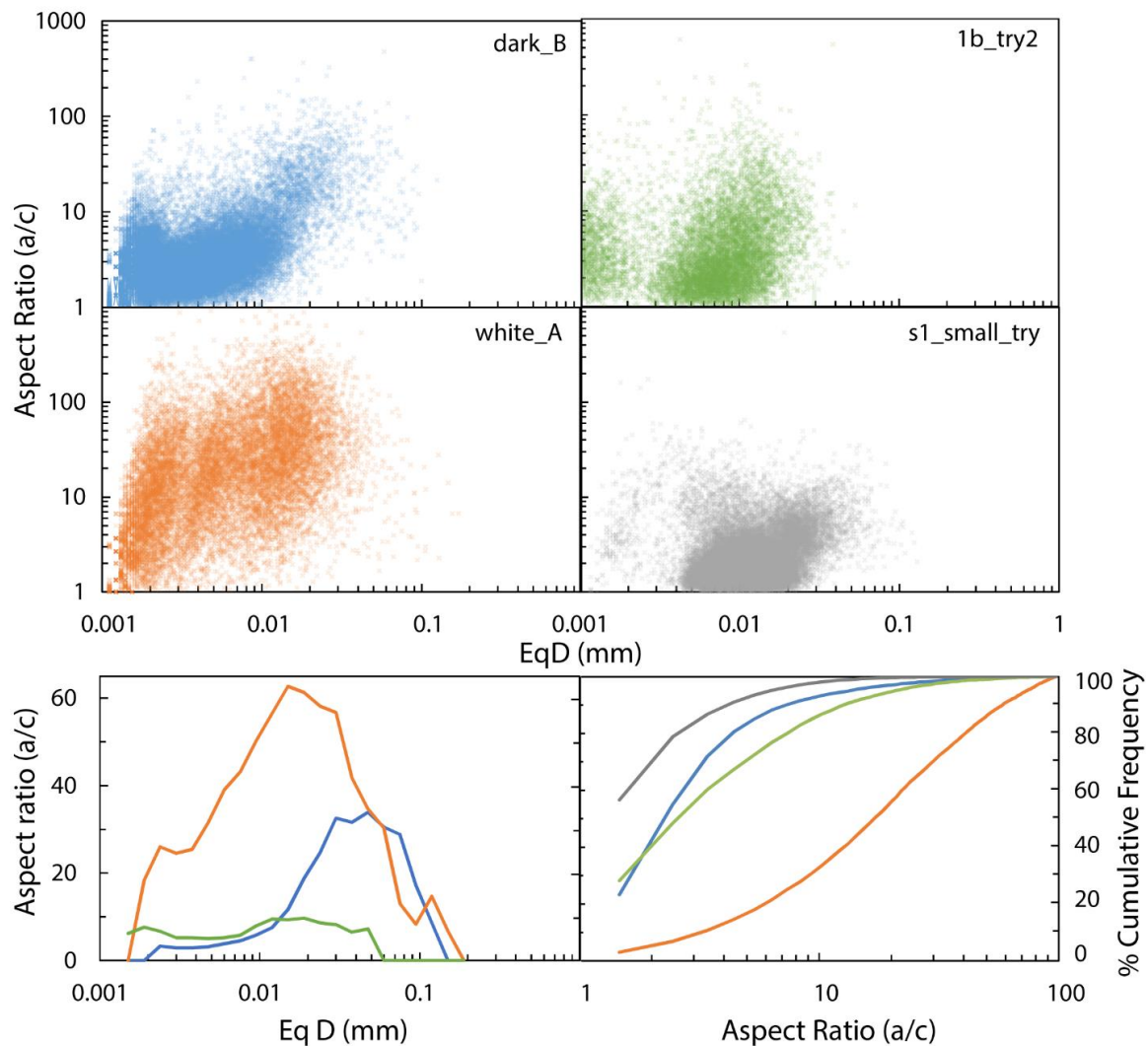
of vesicles in volcanic rocks: An integrated methodology: *Journal of Volcanology and Geothermal Research*, v. 190, p. 271–289, doi: 10.1016/j.jvolgeores.2009.12.003.

Online Resource 5 – X-ray computed microtomography

The fine pumice scans were acquired with monochromatic X-rays at ~ 25 keV and were reconstructed using the TomoPy gridrec algorithm (Gürsoy et al., 2014). The image stacks were then binarized based on greyscale thresholds. Because 3-dimensional porosity is entirely connected in most Havre pumice, a bubble decoalescence technique was used to quantify bubble size distributions and aspect ratios. We used an Avizo step-by-step watershed technique to separate bubbles in 3D, and generate AR (aspect ratio) and bubble size measurements (see Online Resource 3). Watershed separation of highly elongated pumice (e.g., tube pumices) resulted in some vesicle over-separation.

We do two separate types of analyses on 3D XRT images. First, we decoalesce bubbles using a step-by-step watershed technique in Avizo and then measure bubble sizes and aspect ratios (as seen below).

Figure S5i. (Top) Derived aspect ratios (a =maximum, c =minimum) and spherical-volume-equivalent diameter (EqD) for every vesicle analyzed in each 3D XRT core *after* watershedding and vesicle separation. (Bottom) Average aspect ratio with EqD bin sizes of $\times 10^{0.1}$, and the cumulative frequency of aspect ratio starting with a bin size of 1 (spherical) to 2 – plotted at 1.5.



The step-by-step watershed technique we used to decoalesce bubbles is described in detail in the Supplement to [Fauria et al. \(2017\)](#). Briefly, we applied a Gaussian filter before separation was attempted on some data sets, and used a neighborhood value of 26 during the watershed separations. We found that the bubble decoalescence was satisfying for most regular pumice, but did not work on tube pumice. Once the bubble separation was complete, we measured bubble sizes and aspect ratios using the “Label Analysis” module in Avizo. We report 3D aspect ratios (ratio of major to minor axis) of four samples above (**Figure S5i**).

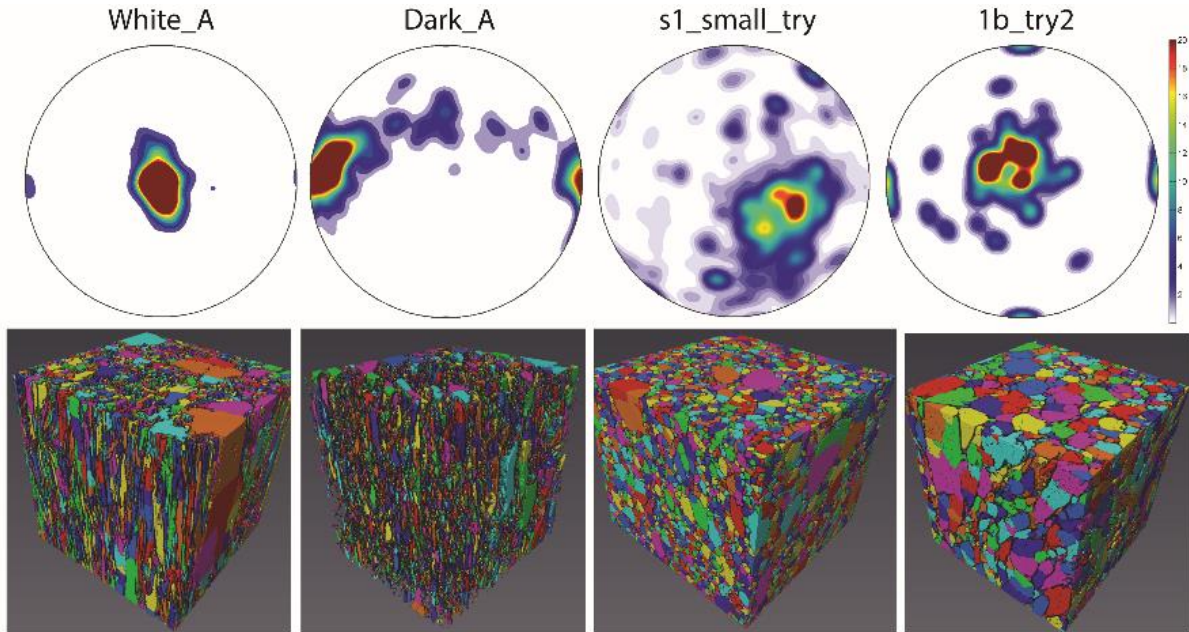
The four samples come from floating Raft Pumice (1b_try2 and s1_small_try) and sunk seafloor pumice in a talus deposit near Dome OP (white_A and dark_A). The AR of every vesicle in the μ XRT scan is plotted against each vesicle’s volume-equivalent spherical diameter (EqD) in the four panels (**Figure S5i**). We also show the average AR for each geometric size bin in the second panel above and assess the frequency of vesicles with a particular AR.

White_A vesicles have distinct elongation that varies with EqD but is captured in part by the watershed analysis (**Figure S5ii**). The low vesicularity of white_A and dark_A (51 and 28% respectively) makes bubble decoalescence more straightforward and robust compared to decoalescence of higher vesicularity tube pumice. Elongate vesicles in white_A and dark_A also display a strong orientation to a particular direction. The two raft samples (1b_try2 and s1_small_try) had less of a preferred vesicle orientation and more consistent aspect ratios where over 80% of the vesicles analyzed have AR <5 (these non-tube samples have 69 and 72% vesicularity). In White_A 80% of vesicles have AR > 5. See 3D renderings (each color corresponds to a different bubble) and pole figures of vesicle orientation and aspect ratios below of each sample. The pole figures, where the scale bar corresponds to aspect ratio, demonstrate that the bubbles are aligned in similar directions. In general, these results demonstrate that many samples contained highly oriented and elongated vesicles and that the degree of elongation can be quantified in 3D by the aspect ratio.

References:

- Fauria, K. E., Manga, M., & Wei, Z. (2017). Trapped bubbles keep pumice afloat and gas diffusion makes pumice sink. *Earth and Planetary Science Letters*, 460, 50-59.
- Gürsoy, D., De Carlo, F., Xiao, X., & Jacobsen, C. (2014). TomoPy: a framework for the analysis of synchrotron tomographic data. *Journal of synchrotron radiation*, 21(5), 1188-1193.

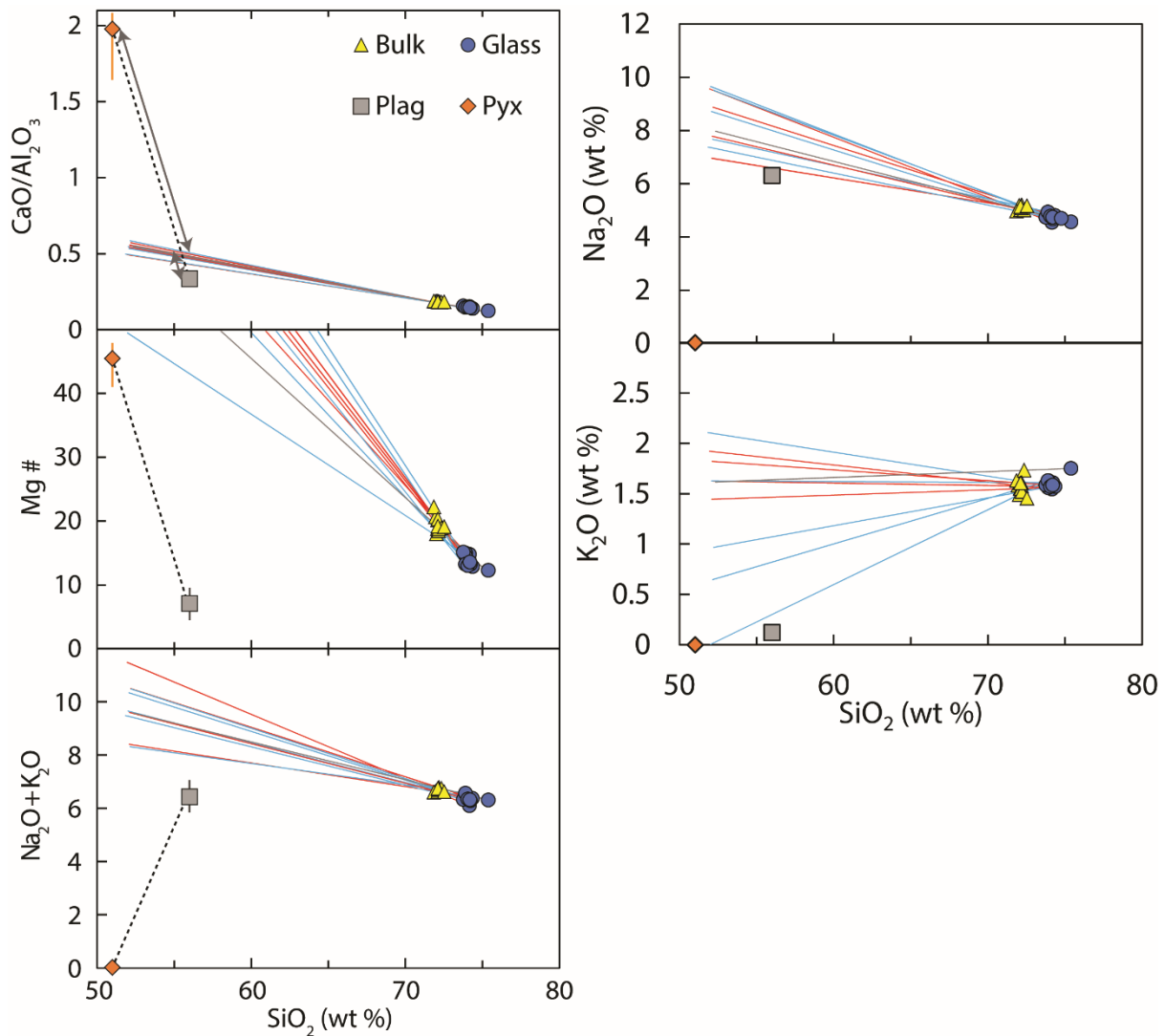
Figure S5ii. Vesicle aspect ratio pole figures and 3D renditions of each XRT pumice core each <3 mm in diameter. Aspect ratio given as a color scale from 1 (purple) to 20 (dark red). The pole figures are entered to the vertical coring axis (as seen below). The 3D core images show individual vesicles separated by color from watershed processing in Avizo.



Online Resource 6 – Alkali metals bivariate plot

Based on major element variations with SiO₂, variations in Ca, Al and Na within glass are attributed to the crystallization of plagioclase and orthopyroxene, both in the phenocryst and microlite assemblages (**Figure 2**). Mg and Fe variations cannot be explained by the crystallization of phenocrysts, but could be explained by the crystallization of orthopyroxene and Fe-Ti oxide microlites not resolvable with EPMA. The grey banding crystallization trends in GP290 match those of other giant pumices. Banding in GP290 appears to be textural rather than due to whole rock composition.

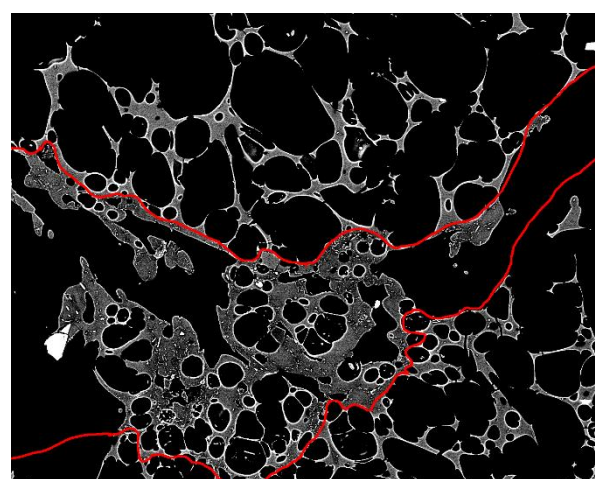
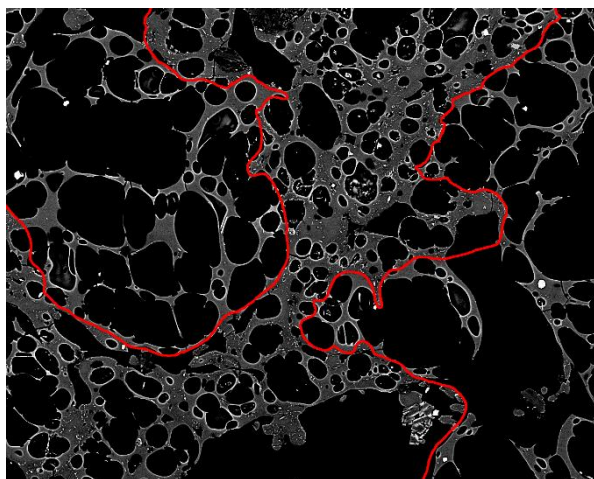
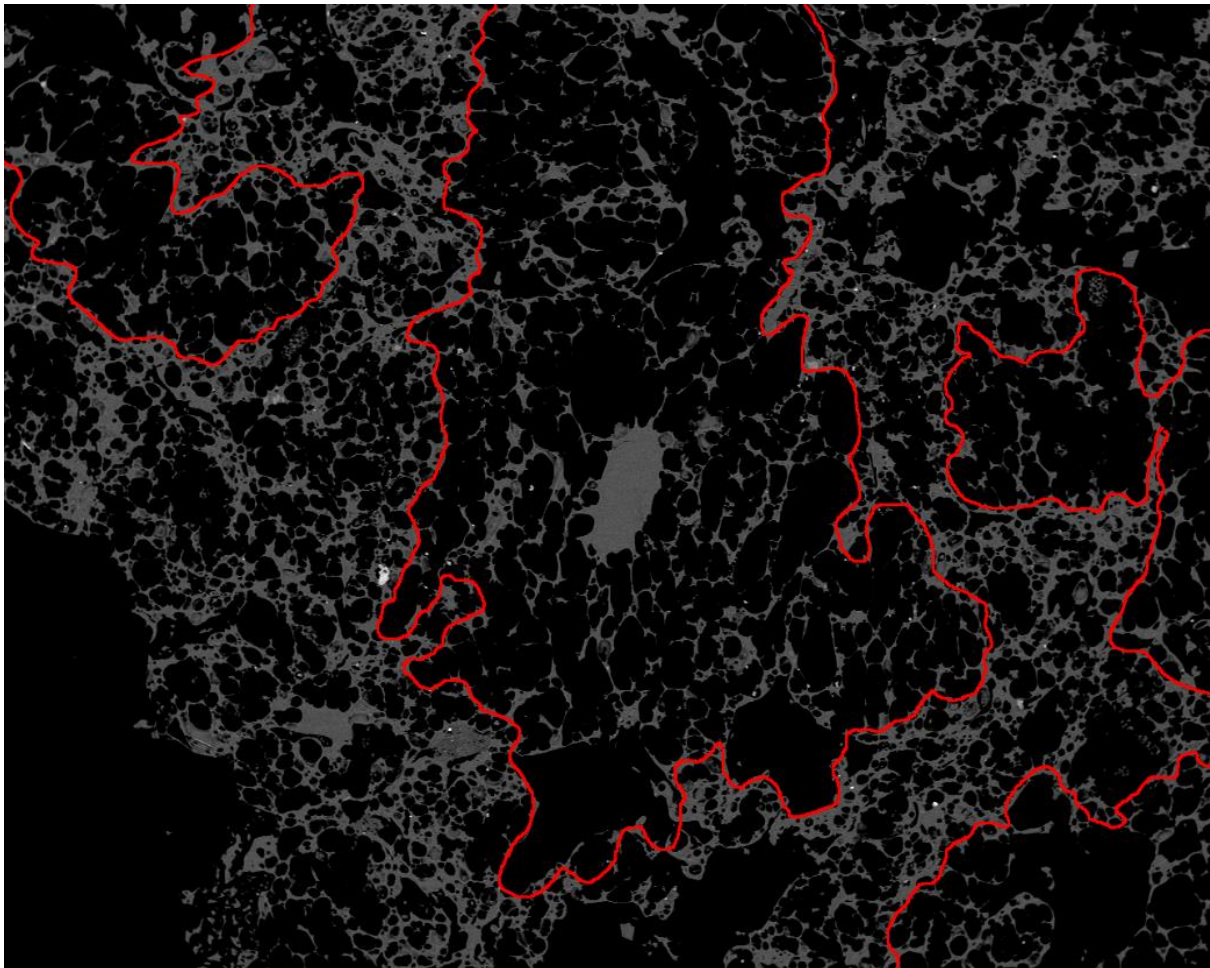
Figure S6i: The lines shown are linear extrapolation bulk-glass chemistry pairs for each sample. The color of the line corresponds to the textural classification (blue = regular, red = tube, grey = banded).



The nucleation and growth of more sodic “albite” feldspar microlites at lower temperature conditions can account for the need of more Na-rich crystal source to produce the determined glass compositions. The growth of Fe-rich oxide microlites could account for the deficit of Fe in the glass chemistry rather than controlled by pyroxene or plagioclase microlite crystallization. All variations from bulk to glass chemistry can be accounted for by the growth of crystal phases rather than any external chemistry or magma mixing.

Online Resource 7 – *Thin sinuous banding (Type 1)*

BSE images of thin, sinuous bands within banded giant pumice exterior. Red lines define the boundaries between the two regions. Bands that appear grey in hand sample exhibit lower 2D vesicularity and increased microlite growth than the surrounding white pumice in thin section. Top image (**Figure S7i**) taken at 50× mag., bottom images (**S7ii-iii**) taken at 200× mag.



Online Resource 8 – Porosity and permeability

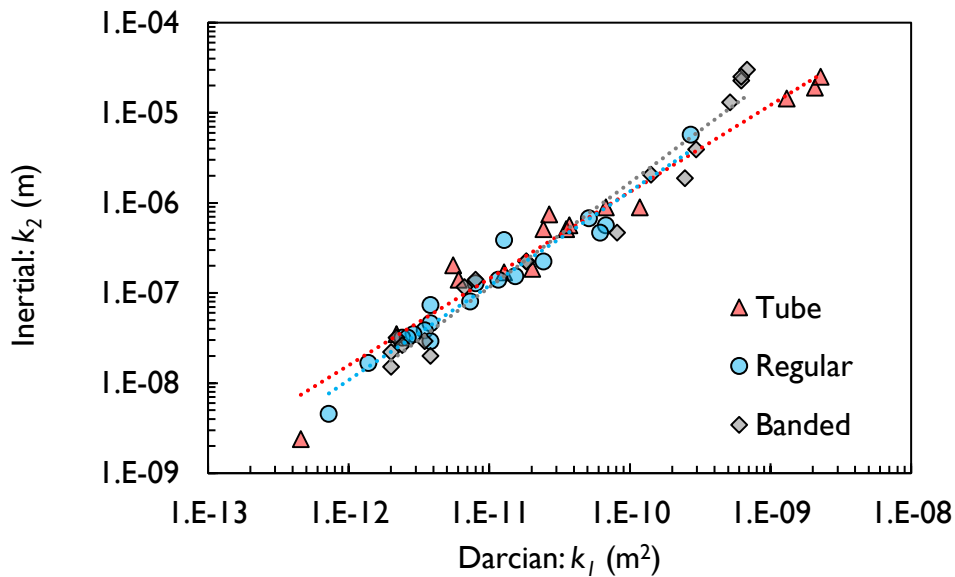
Results from Helium pycnometry and permeability analysis. All Tube cores had a diameter of 19 cm and lengths of 1.1 to 2.7 cm. All other cores had a diameter of 2.2 cm and lengths of 1.0 to 2.9 cm.

k1 (Darcian perm.) and k2 (inertial perm.) were acquired through capillary flow porometry of cylindrical cores. *Data acquired from [Manga et al. \(2018a\)](#). X and Y in the sample names refer to samples taken at perpendicular directions to each other. In Tube samples, Y cores have elongate vesicles parallel to the direction of air flow during capillary flow porometry.

HVR_Sample	Category	Total porosity (%)	Isolated porosity (%)	Connected porosity (%)	Connectivity	$k_1 (m^2)$	$k_2 (m)$
003a	Tube	88.52	1.57	86.95	0.98	-	-
003b		89.94	0.91	89.03	0.99	-	-
003c		90.02	1.27	88.75	0.99	-	-
022Yi		78.25	40.97	37.28	0.48	-	-
022Yii		71.15	-12.88	84.03	1.18	-	-
103X		84.11	3.04	81.07	0.96	4.57E-13	2.38E-09
103Yi		84.84	2.20	82.64	0.97	2.44E-11	5.11E-07
103Yii		84.40	1.54	82.86	0.98	2.67E-11	7.40E-07
103Yiii		85.56	1.54	84.02	0.98	1.30E-09	1.43E-05
115X		84.52	1.13	83.39	0.99	-	-
115Yi		83.17	2.83	80.34	0.97	5.54E-12	2.03E-07
115Yii		85.15	1.90	83.25	0.98	3.53E-11	5.11E-07
115Yiii		84.36	2.27	82.09	0.97	3.72E-11	5.61E-07
121Yi		87.04	1.82	85.21	0.98	2.07E-09	1.89E-05
121Yii		87.41	1.78	85.62	0.98	2.27E-09	2.49E-05
121Yiii		85.23	2.17	83.06	0.97	6.75E-11	8.91E-07
121Yiv		84.35	1.80	82.55	0.98	1.18E-10	8.91E-07
133X		86.52	0.99	85.53	0.99	2.03E-11	1.85E-07
133Y		84.70	1.88	82.82	0.98	1.27E-11	1.68E-07
223Yi		77.59	4.87	72.72	0.94	6.08E-12	1.40E-07
223Yii		75.93	3.15	72.79	0.96	2.20E-12	3.49E-08
281Xi		84.99	2.47	82.52	0.97	7.23E-13	4.55E-09
281Xii		85.31	1.83	83.48	0.98	1.38E-12	1.66E-08
281Xiii		85.04	2.32	82.72	0.97	3.83E-12	4.61E-08
281Yi		85.54	1.67	83.88	0.98	-	-
281Yii		87.12	1.50	85.62	0.98	-	-
041Yi	Regular	83.49	2.83	80.66	0.97	6.75E-11	5.61E-07
041Yii		85.49	1.95	83.54	0.98	6.15E-11	4.66E-07
096Yi		88.85	0.95	87.89	0.99	3.49E-12	3.83E-08
096Yii		89.87	0.57	89.30	0.99	2.90E-12	3.49E-08
106		87.38	0.79	86.59	0.99	2.44E-11	2.22E-07
125X		89.43	-0.32	89.76	1.00	3.83E-12	7.32E-08
125Y		88.40	0.46	87.94	0.99	3.83E-12	2.90E-08
164Yi		68.37	3.78	64.59	0.94	7.32E-12	8.03E-08
192a		90.18	0.48	89.70	0.99	1.27E-11	3.87E-07
192b		90.14	0.52	89.62	0.99	5.11E-11	6.75E-07
192c	89.83	0.34	89.49	1.00	2.71E-10	5.67E-06	
221	84.42	2.86	81.57	0.97	1.53E-11	1.53E-07	
227Xi	78.51	4.02	74.49	0.95	-	-	
227Xii	82.76	3.26	79.50	0.96	8.03E-12	1.27E-07	
227Y	82.53	2.28	80.25	0.97	1.16E-11	1.40E-07	
*227_a	85.74	1.62	84.12	0.98	2.27E-10	1.37E-06	
*227_b	85.09	1.80	83.30	0.98	5.39E-12	4.70E-08	
231a	79.76	3.28	76.47	0.96	2.41E-12	3.18E-08	
231b	80.71	2.32	78.38	0.97	2.64E-12	3.18E-08	
*262_a	87.25	1.17	86.08	0.99	8.17E-12	1.24E-07	
*262_b	87.40	-2.19	89.59	1.03	3.10E-12	3.25E-08	
044a	Banded	81.56	3.63	77.94	0.96	8.03E-12	1.40E-07
044b		79.94	4.57	75.37	0.94	1.85E-11	2.22E-07
044c		81.34	3.94	77.41	0.95	1.83E-11	2.22E-07

139a		82.92	2.47	80.45	0.97	2.00E-12	2.20E-08
139b		84.41	2.10	82.32	0.98	2.20E-12	3.18E-08
139c		83.02	2.84	80.18	0.97	2.41E-12	2.64E-08
139d		79.81	4.28	75.53	0.95	3.83E-12	2.00E-08
165X		87.75	-0.39	88.14	1.00	8.12E-11	4.66E-07
165Yi		85.92	1.48	84.45	0.98	1.42E-10	2.05E-06
165Yii		82.94	2.78	80.16	0.97	5.17E-10	1.30E-05
226a		79.45	2.73	76.72	0.97	6.22E-10	2.27E-05
226b		81.67	2.44	79.23	0.97	2.47E-10	1.87E-06
243a		81.30	3.20	78.10	0.96	2.97E-10	3.92E-06
243b		80.11	3.64	76.47	0.95	6.83E-10	3.00E-05
267Yi		81.85	2.98	78.87	0.96	6.67E-12	1.16E-07
267Yii		81.50	2.99	78.51	0.96	6.22E-10	2.49E-05
278a		81.61	1.85	79.76	0.98	3.49E-12	2.90E-08
278b		79.06	2.61	76.45	0.97	2.00E-12	1.52E-08
*290	Banded	78.21	-0.70	78.91	1.01	1.18E-12	5.36E-09
*"	GP290	80.31	-0.93	81.25	1.01	1.43E-10	3.75E-07
*"		78.62	0.28	78.34	1.00	1.23E-12	5.62E-09
*"		74.80	1.66	73.14	0.98	1.13E-11	7.80E-08
*"		79.49	0.34	79.15	1.00	2.14E-12	9.33E-09
*"		74.73	1.19	73.54	0.98	1.42E-11	1.36E-07
*"		80.55	-0.10	80.65	1.00	3.10E-12	1.55E-08
*"		79.59	-0.04	79.63	1.00	3.40E-12	2.83E-08
*"		60.90	24.91	35.99	0.59	-	-
*"		79.93	0.02	79.91	1.00	9.33E-13	8.91E-09
*"		78.50	-0.09	78.59	1.00	1.49E-11	1.62E-08
*"		77.69	1.30	76.40	0.98	2.96E-12	7.76E-09
*"		79.24	0.44	78.80	0.99	2.96E-12	2.35E-08
*"		78.73	0.91	77.82	0.99	1.86E-12	1.18E-08
*"		76.63	1.68	74.95	0.98	2.35E-12	1.29E-08
*"		80.23	0.55	79.67	0.99	1.42E-11	1.56E-07
*"		80.28	0.41	79.87	0.99	5.65E-12	7.80E-08
*"		79.94	0.41	79.53	0.99	3.25E-12	4.09E-08
*"		78.06	0.76	77.29	0.99	1.62E-12	6.75E-09
*"		83.02	-1.16	84.18	1.01	1.08E-11	7.45E-08
*"		78.71	-2.04	80.75	1.03	1.48E-12	3.71E-09
*"		77.04	-0.38	77.41	1.00	3.25E-12	4.48E-08
*"		77.15	-0.65	77.79	1.01	1.18E-12	3.71E-09
*"		77.39	-0.60	77.99	1.01	1.30E-11	1.30E-07
*"		80.16	-1.33	81.49	1.02	2.05E-12	1.23E-08
*"		77.90	-0.29	78.19	1.00	1.95E-12	1.23E-08
*"		76.74	-0.39	77.13	1.01	3.56E-12	1.07E-08

Figure S8i: Comparison of Darcian and inertial permeability.



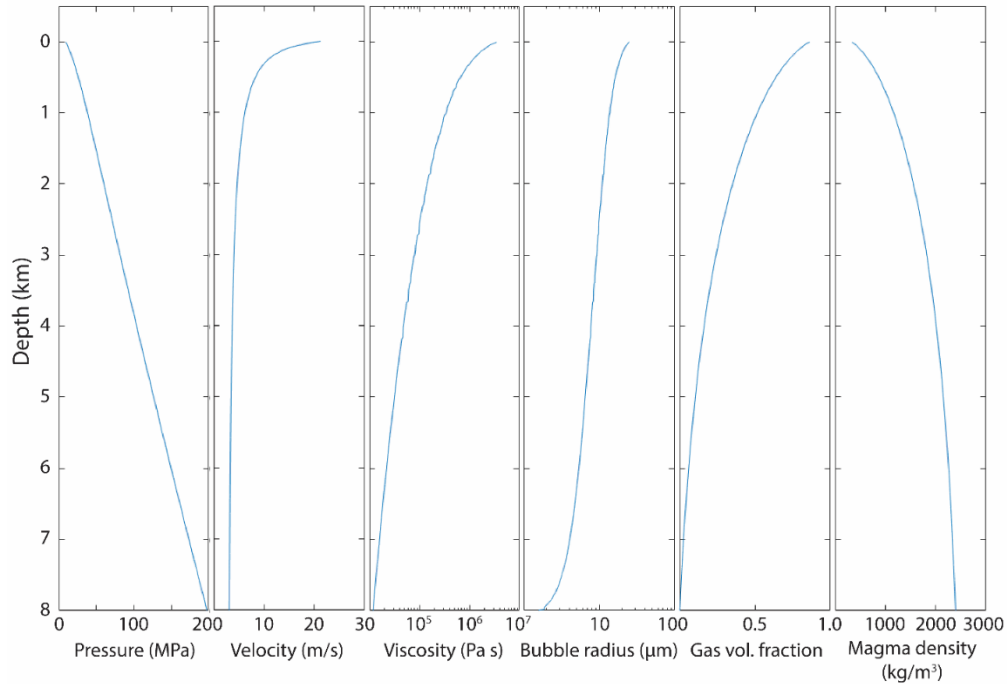
Online Resource 9 – *Microlite phase number densities*

Breakdown of microlite number densities per area for all giant pumice samples including different microlite phases identified: Plagioclase feldspar, Fe-Ti oxides, pyroxenes and quartz. BSE images analyzed at 250, 500 and 1000 times magnification.

Sample (HVR_)		3	22	41	96	115	192	221	231	270	290	290I
Images analyzed		2	6	4	6	5	3	4	6	7	5	5
Total melt area (mm ²)		0.02	0.05	0.03	0.05	0.03	0.01	0.13	0.07	0.06	0.01	0.05
Total area (mm ²)		0.09	0.14	0.19	0.42	0.23	0.14	0.46	0.28	0.22	0.04	0.13
Vesic. (%)		78.84	65.72	81.39	87.27	85.73	89.45	70.97	74.96	73.41	62.48	67.25
Phase (mN)	Plag	2	23	101	4	7	1	22	31	19	505	527
	Oxide	44	623	816	141	444	31	811	1084	604	1367	1684
	Pyx.	0	14	38	7	32	4	59	25	1	45	63
	Quartz	0	1	0	0	0	2	0	0	0	0	0
Total mN		46	661	955	152	483	38	892	1140	624	1917	2274
Phase (mN _A) (mm ⁻²)	Plag	101	468	2907	86	210	68	174	442	320	34684	11168
	Oxide	2229	12675	23489	3026	13337	2100	6404	15461	10160	93887	35686
	Pyx.	0	285	1094	150	961	271	466	357	17	3091	1335
	Quartz	0	20	0	0	0	135	0	0	0	0	0
Total mN _A (mm ⁻²)		2330	13449	27490	3263	14509	2574	7044	16260	10496	131662	48188
Corrected Phase (mN _A cr) (mm ⁻²)	Plag	21	165	541	10	30	7	48	111	86	12594	4108
	Oxide	472	4479	4373	338	1903	221	1759	3871	2733	34090	13125
	Pyx.	0	101	204	17	137	29	128	89	5	1122	491
	Quartz	0	7	0	0	0	14	0	0	0	0	0
mN _A (cr) (mm ⁻²)		493	4752	5118	364	2070	271	1935	4071	2824	47805	17724

Online Resource 10 – Strain model results

Figure S10i: Results of the 1D conduit ascent model (Manga et al., 2018a) when reapplied into the strain model for magma pressure, mean bubble radius, magma viscosity, gas fraction and bulk magma density vs. conduit depth. Initial conditions are set as crystal fraction = 0.05, initial H₂O content of 5.8 wt%, bubble number density of $2 \times 10^8 \text{ cm}^{-3}$, conduit depth of 8 km, initial storage pressure of 200 MPa, melt density of 2400 kg m^{-3} , mass eruption rate = 10^7 kg s^{-1} (Carey et al., 2018), of and a vent pressure of 10 MPa.



We also note that the vesicle size chosen affects the capillary number and expected aspect ratio. Below (Figure S10ii) is an example of how aspect ratios may be expected to change across the very top of conduit (0 m ≡ 900 mbsl) with a changing vesicle size from 1 μm to 1 mm. The actual predicted vesicle diameter at this point in the conduit (4 m below the 900m deep vent) from the Manga et al. (2018a) model is 25 μm (-4.6 log(m)).

